Energy
Advances

Graphite

ZnO

ROYAL SOCIETY
OF **CHEMISTRY**

PAPER
Xinhua Liang *et al.*
Graphite particles modified by ZnO atomic layer deposition
for Li-ion battery anodes

ROYAL SOCIETY
OF CHEMISTRY

Check for updates

Graphite particles modified by ZnO atomic layer deposition for Li-ion battery anodes†

Ahmad Helaley, [ID] [a] Han Yu [b] and Xinhua Liang [ID] *[a]

Graphite, with a modest specific capacity of 372 mA h g^{-1}, is a stable material for lithium-ion battery anodes. However, its capacity is inadequate to meet the growing power demands because the formation of an irregular solid electrolyte interphase (SEI) can result in unstable performance. In this research, we used a few cycles of atomic layer deposition (ALD) to deposit ZnO on graphite particles as an anode with improved electrochemical stability. Transmission electron microscopy revealed that ZnO was in the form of nanoparticles due to the inert surface properties of graphite and only a few cycles of ALD. Electrochemical characterization demonstrated that the ZnO ALD nanoparticles significantly inhibited dendrite growth, and X-ray photoelectron spectroscopy revealed that side reactions at the electrolyte–electrode interface were inhibited with the deposition of ZnO. The SEI layer was stabilized, which improved the cycling stability of the ZnO–graphite composite electrode. The electrode made of graphite with 2 cycles of ZnO ALD had about 20% higher discharge capacity than that of pristine graphite, and it remained stable at 420 mA h g^{-1} after 500 cycles of charge/discharge. This surface modification technique can significantly increase the potential use of widely available graphite composites for high-performance batteries.

Introduction

Lithium-ion batteries (LIBs), currently the most widely used rechargeable batteries, offer the benefits of small size, high energy density, highly reversible cycling, minimal self-discharge, and no memory effects.[1] However, some challenges remain and limit the further applications of LIBs, such as the formation of lithium dendrites, irregular formation of a solid electrolyte interphase (SEI), volume changes, and side reactions.[2] The formation of dendrites can create a thick SEI and increase Li-ion consumption. Additionally, dendrites produce dead lithium, creating an irreversible capacity loss and sharply lowering energy density; they can also cause interior short circuits, propagation of thermal runaway, gas venting, and explosions.[3,4]

Although graphite-based anodes are extensively used as LIB anodes,[5] their moderate theoretical capacity is unlikely to satisfy the increasing power demands of electric-powered vehicles, aircraft, and grid-scale storage.[4,6–11] It is desirable to

enhance the performance of widely available graphite. In electrodes, the SEI layer exposed to the electrolyte must be both electrically insulating and permeable to Li-ions in order to limit electrolyte decomposition during charge/discharge cycling.[5,7,12–21] If the SEI layer grows too thick, fewer Li-ions can be inserted, causing increased resistance to Li-ion penetration into graphite and decreased reversible capacity. To realize the full potential of graphite electrodes, it is essential to reduce dendrite growth and control the thickness of the SEI layer, thus improving their electrochemical properties.[1,22–26]

Significant research has sought novel, low cost anode materials that are not dependent on an intercalation mechanism and can offer higher energy density, higher power density, and longer lifetimes.[3,11,22,27,28] Zinc oxide (ZnO) is one such substance, and it has a higher Li-ion diffusion coefficient and allows Li-ions to diffuse readily. The theoretical discharge capacity of ZnO (987 mA h g^{-1}) is nearly three times that of graphite (372 mA h g^{-1}), making it a potential candidate for rechargeable Li-ion battery anodes, compared to the other transition metal oxides.[8] However, due to their significant volume expansion (228%) during charge/discharge cycling, ZnO electrodes lose stable contact with the current collector and experience electrode pulverization, leading to quick capacity fading.[8,23,29–31] This volume change leads to early capacity loss, affects rate capability, and compromises safety.[7,32–36] Because ZnO and other transition metal oxides cannot resolve this inherent stability issue, they are ultimately not appropriate for real-world applications in their bulk form. Applying highly

a Department of Energy, Environmental and Chemical Engineering, Washington University in St. Louis, St. Louis, MO 63130, USA.
E-mail: xinhua.liang@wustl.edu

b Linda and Bipin Doshi Department of Chemical and Biochemical Engineering, Missouri University of Science and Technology, Rolla, MO 65409, USA

dispersed ZnO nanoparticles or ultra-thin films can overcome the issue of volume expansion and improve Li-ion transport while resolving the stability issue.[37,38]

Atomic layer deposition (ALD) is a layer-by-layer thin film coating technology and it has been used to modify the surface of electrodes or electrode particles. This work focuses on the performance enhancement of graphite particles by ZnO ALD. Only a few cycles of ALD were used to deposit ZnO on graphite particles, and the obtained composite particles were systematically characterized and evaluated as anodes for LIBs. Due to the limited number of ALD cycles and the inert nature of the graphite surface, ZnO was deposited on the graphite particle surface as nanoparticles, not one continuous layer of film. Normally, a conformal film will be formed when deposited through a sufficient number of ALD cycles.[11,38] The capacity of graphite electrodes is often lower than their theoretical capacity due to various factors, such as side reactions and the formation of an unstable SEI layer. In this study, the deposited ZnO nanoparticles acted as a physical barrier, inhibiting the growth of lithium dendrites during charge/discharge cycling, thereby enhancing the electrode's long-term cycling performance. ZnO ALD also facilitated the transport of lithium ions within the electrode, improving the kinetics of the intercalation and de-intercalation processes. This improvement in ion mobility leads to a notable increase in capacity and enhanced rate capability.

Experimental section

ZnO ALD on graphite particles

ZnO ALD on graphite particles was carried out in a fluidized bed reactor. Diethylzinc (Sigma Aldrich) and deionized water, used as precursors for Zn and O, respectively, were delivered into the reactor by their vapor pressures at room temperature. In a typical ZnO ALD cycle, diethylzinc was first fed into the reactor and interacted with functional groups on the particle substrate surface. When the surface reaction was completed, diethylzinc flowing into the reactor was halted, and nitrogen gas was fed into the reactor to remove unreacted diethylzinc and any byproducts from the reactor chamber. In the second half reaction, water vapor was then fed into the reactor, removing the ethyl groups from the adsorbed diethylzinc and leaving a hydroxide group on the substrate surface, and nitrogen gas was fed into the reactor to remove unreacted water and any byproducts from the reactor system. By repeating this process, we can deposit ZnO with a precisely controlled amount on the surface of the graphite particles. The reactor temperature was 200 °C. The dosage duration, purging time, and inert gas flow rate were controlled by LabVIEW software. Various amounts of ZnO were deposited by varying the number of ALD cycles (e.g., 0, 2, 5, and 10 cycles of ZnO ALD), and the samples were labeled as UC–graphite, 2Zn–graphite, 5Zn–graphite, and 10Zn–graphite, respectively.

Electrode preparation and coin cell assembly

The working electrode was prepared by mixing graphite and/or ZnO–graphite composite particles with carbon black (CB; Alfa Aesar), polyvinylidene fluoride (PVDF; Sigma-Aldrich) with a

mass ratio of 85 : 5 : 10 and N-methyl-2-pyrrolidone (NMP; Sigma-Aldrich). The resulting slurry was uniformly coated on copper foil with a doctor blade (MTI Corp.), then first dried on a heated platform at 90 °C for a few minutes and then in a vacuum oven at 120 °C overnight. Finally, electrode disks with a mass loading of about 3 mg cm^{-2} were punched out of the coated foil. A 2032-type coin cell was assembled at ambient temperature in a glove box that was filled with argon (oxygen and moisture concentrations of less than 0.1 ppm). The counter electrode was a 15 mm diameter Li–metal foil disk (99.9% trace metals basis, Sigma-Aldrich). The electrolyte was a solution of 1 M LiPF$_6$ in ethyl methyl carbonate/ethylene carbonate (EMC/EC, 1 : 1 by volume), and the separator was a porous tri-layer polymer made of polypropylene (PP)/polyethylene/PP (Celgard Inc.).

Electrochemical measurements

A NEWARE battery tester with a voltage range of 0.01–1.5 V was used for the electrochemical testing at room temperature. The first two cycles of charge/discharge were conducted at a current density of 0.1C (1C = 372 mA g^{-1}). Galvanostatic analysis was carried out to assess the electrochemical characteristics of the assembled coin cells. Electrochemical impedance spectroscopy (EIS) was carried out using a potentiostat (SPE-150, BioLogic) with an impedance spectrum ranging from 1 MHz to 10 mHz and an amplitude of 5 mV after coin cells were fully discharged; cyclic voltammetry (CV) was carried out within a potential range of 0–2.5 V and a screening rate of 0.1 mV s^{-1}.

Material characterizations

X-ray photoelectron spectrometry (XPS, Kratos Axis 165, monochromatic AlK radiation source) was used to determine the elemental composition of the electrodes before and after cycling. Scanning electron microscopy (SEM) was used to investigate the morphology and microstructure of the electrode and bare graphite-based anode materials using field emission SEM (FEI Helios Nano Lab 600). Transmission electron microscopy (TEM) was carried out with a JEOL JEM-2100F field-emission STEM and a Bruker SDD energy dispersive X-ray (EDX) spectrometer to directly observe the existence and morphology of ZnO on graphite particles. The compositions and crystal structure of the active materials were analyzed by using Fourier transform infrared spectroscopy (FTIR, Nicolet IS50) and X-ray diffraction (XRD, Bruker d8 X-ray Diffractometer), respectively.

Results and discussion

Pristine graphite and ZnO–graphite composite powders were analyzed by FTIR. This analytical approach was used to investigate the chemical composition and molecular structure of these materials, providing insights into the role of functional groups. As shown in Fig. S1 in the ESI,† both pristine graphite and ZnO modified graphite powders exhibited multiple peaks, including those at around 1342 cm^{-1} and 1183 cm^{-1}, indicative of asymmetric C–C stretching within the graphite, and the bending vibration of C–H from the alkane group. FTIR analysis

provides bonding information between ZnO and graphite. A very weak peak at 431 cm^{-1} in the ZnO–graphite composite was attributable to the Zn–O stretching vibration of the Zn–O–C bond. To gather more information, we performed XRD and XPS studies.

The crystallinity of the ZnO–graphite composite and the pristine graphite powders was assessed using XRD. As shown in Fig. 1, the XRD pattern of UC–graphite showed two diffraction peaks at 26.74° and 43.20°, which correspond to the feature peaks (002) and (101) of graphite, respectively. The composite powders exhibited distinct and well-defined diffraction peaks corresponding to the structure of ZnO, consistent with prior ZnO ALD research.[8,10,11] Notably, no shift in the primary graphite peak (002) was observed, confirming that the structural integrity of the graphite substrate was maintained during

the ALD process. The diffraction peaks at 2θ = 36.2°, 37.8°, 44.09°, 58.6°, 64.8°, 65.7°, and 68.4° are assigned to (002), (101), (102), (110), (103), (112), and (201) planes of ZnO. As the number of ALD cycles increased, the characteristic peaks of ZnO became more obvious due to the increased ZnO amount.

TEM was utilized to investigate the morphology and microstructure of ZnO deposited graphite particles. As expected, no continuous layer of ZnO films was formed, due to the inert nature of the graphite surface without many functional groups and the ZnO nanoparticles are expected to grow on defect sites, especially edges with functional groups. In general, with the increase in the number of ALD cycles, a continuous layer of film could form.[8,9,30] Fig. 2a shows low-magnification TEM images of the 10Zn–graphite sample. ZnO nanoparticles with varying sizes from 2 nm to 11 nm were clearly observed on graphite particles with different cycles of ZnO ALD, as shown in Fig. S2 (ESI†). The average particle size did not change much with the increase of the number of ALD cycles; 2.6 ± 0.2 nm for 2Zn–graphite, 2.9 ± 0.6 nm for 5Zn–graphite, and 2.9 ± 0.7 nm for 10Zn–graphite (Note: the particle size distribution does not show particles smaller than 2 nm due to the TEM device's detection limit). The consistent particle sizes observed in this study, particularly for fewer ALD cycles, are advantageous for enhancing the surface area and ion transport. However, with a higher number of ALD cycles, a broader particle size distribution suggests some degree of particle aggregation during ZnO ALD, which may impact the interfacial properties and performance. The small and consistent particle sizes observed in this study may contribute to improved material properties, as smaller particles often enhance the surface area and ion transport.
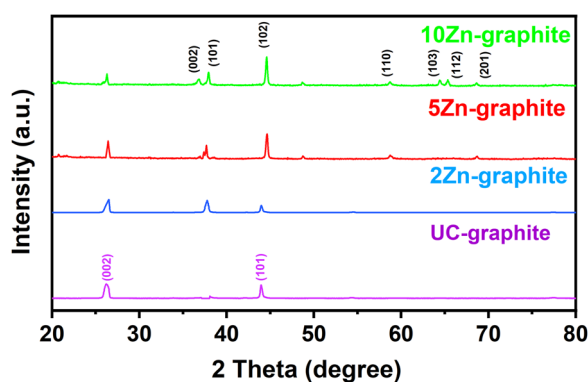

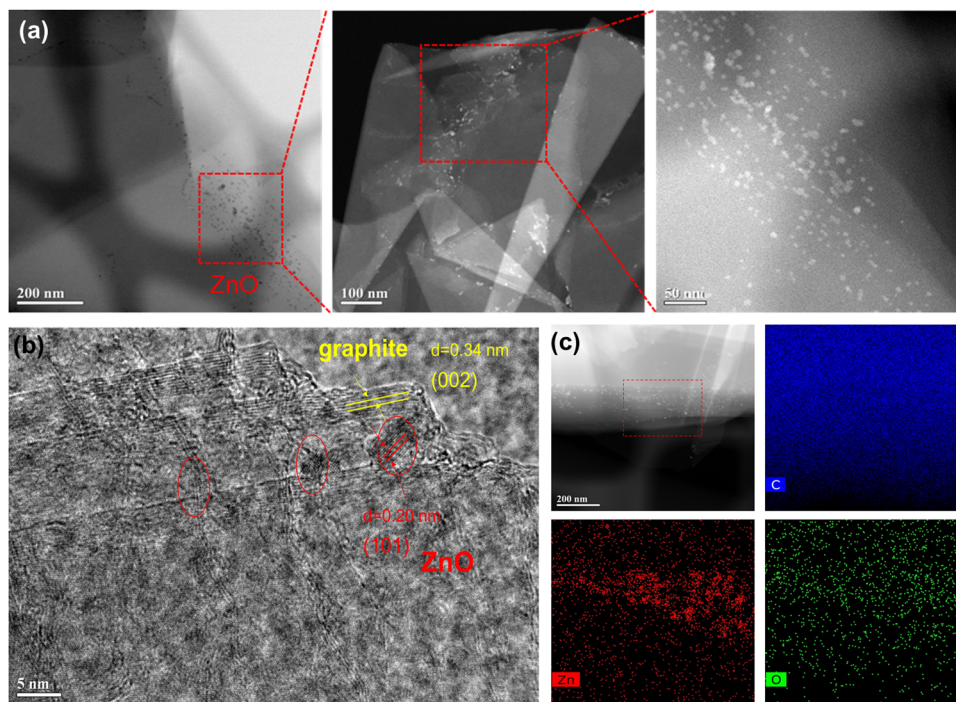Fig. 1 XRD profiles of pristine and coated graphite powders.

Fig. 2 (a) Low magnification of TEM images and (b) high-resolution TEM image of 10Zn–graphite powders, and (c) EDX mapping of 10Zn–graphite powders.

However, further studies or theoretical models are required to fully substantiate their role in advanced battery applications.

In this study, we can safely say that ZnO nanoparticles should be formed on these samples with the number of ALD cycles fewer than 10. A high-resolution TEM image displayed as Fig. 2b reveals the lattice of ZnO with a space of 0.20 nm that is ascribed to the (101) plane of ZnO. Yellow lines indicate the graphite crystal plane with a space of 0.34 nm corresponding to the (002) plane between two single graphene layers in graphite, which is consistent with the XRD findings. This indicates that some of the graphite surface coordinated oxygen functional groups transferred to ZnO lattice sites during the deposition process as a substitute for oxygen vacancies, resulting in the

formation of C–O–Zn bonds in the composite. Fig. 2c shows EDX elemental mapping of 10Zn–graphite, which confirms the element distribution of Zn, indicating that ZnO was successfully deposited on graphite particles using ALD with a consistent distribution of ZnO throughout a population of particles.

Cyclic voltammetry and EIS measurements were used to investigate the SEI formation and growth, internal resistance, and charge transfer resistance of electrodes. We examined the CV curves to determine various properties, such as peak positions and peak currents. These variables can reveal details about the chemical reactions taking place at the electrode surface. In order to fully understand the lithium-ion insertion and extraction processes within the composite material, we
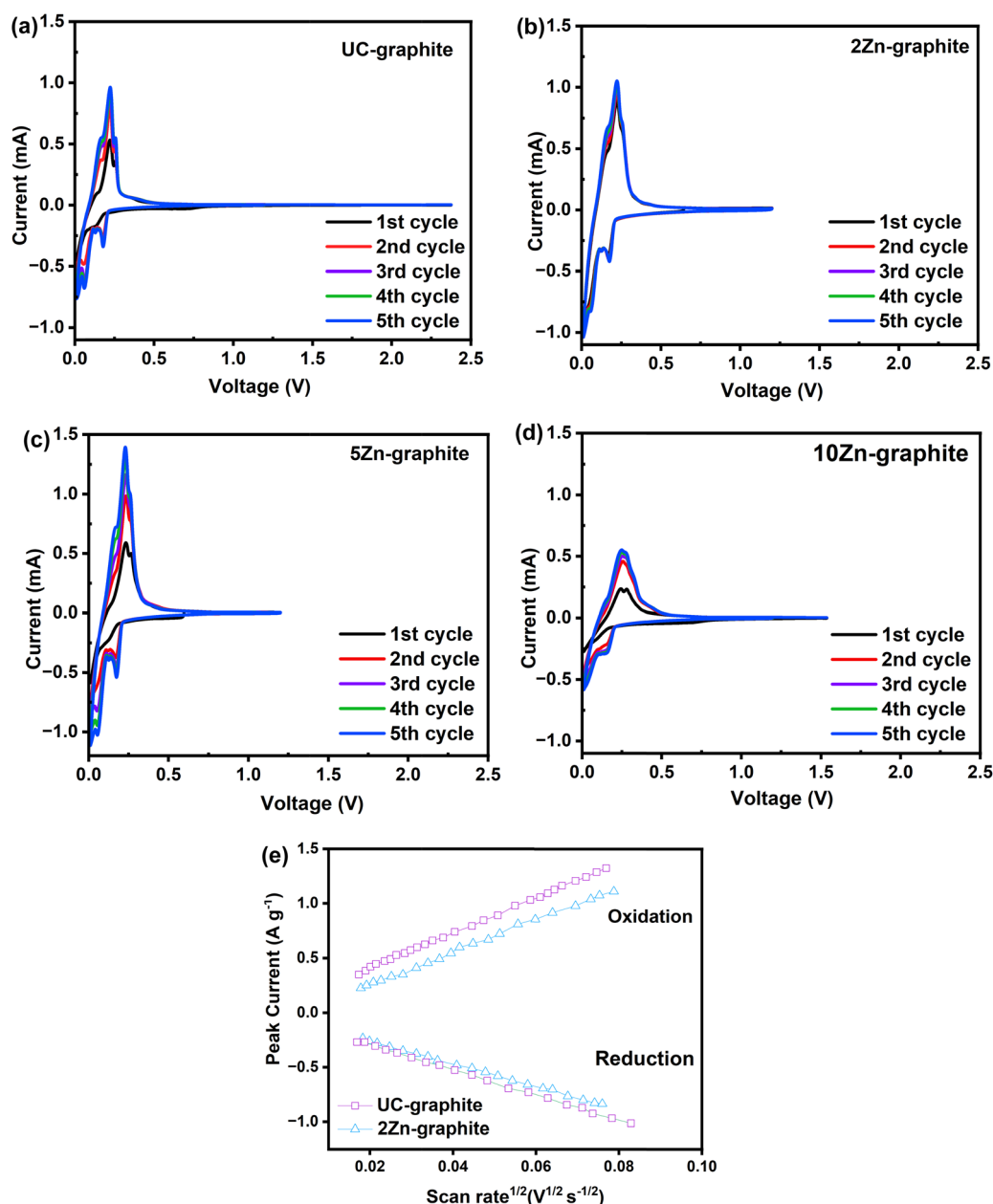

Fig. 3 CV curves of the first five cycles of charge/discharge at 0.1 mV s^{-1} for electrodes made of (a) UC–graphite, (b) 2Zn–graphite, (c) 5Zn–graphite, (d) 10Zn–graphite, and (e) peak current vs. the square root of the scan rate for graphite electrodes.

looked at the redox peaks and their positions on the potential axis. CV curves were used to evaluate the kinetics and reversibility of Li-ion intercalation in both pristine graphite and ALD ZnO–graphite composite electrodes for the first five cycles of charge/discharge at a scan rate of 0.1 mV s^{-1}. The anode potential window ranged from 2.5 V to 0.01 V vs. Li^{+}/Li, as shown in Fig. 3a, and then swept back to 2.5 V, which reflects the potential range under typical battery operation. For all five cycles, the oxidation peak for both pristine and composite electrodes remained at ∼0.2 V; all electrodes showed a dramatic increase in the current during cycling, but it was higher in the composite electrodes except for the 10Zn–graphite electrode, for which it was lower, as shown in Fig. 3. This behavior indicates that Li-ion transport during the lithiation/de-lithiation process was faster in 2Zn–graphite and 5Zn–graphite composite electrodes, which is similar to other phenomena reported previously.[30,39]

In the first cathodic scan, the electrodes made of ZnO ALD modified graphite particles showed a slightly wider reduction peak at around 0.23 V, as shown in Fig. 3b–d. Due to the reduction process, ZnO reacts with Li-ions to produce stable compounds, such as amorphous Li$_2$O (ZnO + 2Li^{+} + 2e^{-} ↔ Zn + Li$_2$O; specific capacity = 658 mA h g^{-1}).[29] The additional capacity (>372 mA h g^{-1}) may result from this reaction. These stable compounds can become part of the SEI layer, improving its robustness and reducing continuous SEI layer growth, which consumes lithium and the electrolyte. However, the volume change from the ZnO conversion reaction in the samples with a high number of ALD cycles may lead to contact loss or decomposition.[9] The anodic scan of the modified electrodes (2Zn–graphite, 5Zn–graphite, and 10Zn–graphite) revealed several oxidation peaks in the potential range of 0.15 V to 0.35 V, which could be related to the decomposition of the SEI layer and the subsequent formation of ZnO from Li$_2$O.[5,6]

However, as illustrated in Fig. 3a and b, the amplitude of the current peak of the 2Zn–graphite was greater than that of the UC–graphite, where both electrodes have the same thickness. This could be the result of the improvement of the de-intercalation of Li-ions and the cell capacity increase and reversibility of the ZnO modified anode material. This finding can be attributed to the specific properties of the low amount of ZnO ALD, which may impact the kinetics of SEI formation during the initial cycles of charge/discharge. The size of these ZnO nanoparticles was smaller than those reported in other studies.[9,11] This offers a higher surface area-to-volume ratio, which is crucial for enhancing electrochemical reactions. This higher surface area can lead to improved battery performance by providing more active sites for lithium ion intercalation, resulting in faster kinetics. ZnO ALD may prevent localized electrolyte decomposition and SEI layer formation, which enhances the SEI layer stability. The current peak amplitude was also greater than that of 10Zn–graphite (Fig. 3d), resulting from the larger amount of ZnO nanoparticles that could store Li-ions; however, a larger amount of ZnO nanoparticles may lead to aggregation of nanoparticles, which can compromise the structural integrity of the electrode. 5Zn–graphite offered a trade-off between Li-ion conductivity/buffering and storage. In the

composite electrodes, there were no extra peaks found in the initial lithiation/delithiation process at 0.55 V and 1.33 V, confirming that there were no alloying/dealloying processes of Li$_x$Zn alloys, as confirmed by the XPS results. Because the lithiation reaction occurred in the same potential window of graphite as that of the zinc reaction with lithium, no zinc alloys formed, so no heat treatment of the deposited ZnO was required.

To explore the lithium-ion diffusion properties, CV measurements were performed on graphite electrodes at scan rates ranging from 0.1 mV s^{-1} to 1.0 mV s^{-1} (refer to Fig. S3 in the ESI†). Fig. 3e illustrates a linear relationship between the peak current (I_p) and the square root of the scan rate ($\nu^{1/2}$) for these electrodes, implying a semi-infinite linear diffusion during cycling. The Randles–Sevcik equation was used to calculate the diffusion coefficient (D) for the materials, with I_p representing the number of electrons involved in intercalation (n), A representing the surface area of the electrode per unit weight of active materials, C representing the concentration of lithium ions within the active materials, ν representing the scan rate, and D representing the resulting diffusion coefficient, as shown in eqn (1). Table 1 shows the apparent lithium-ion diffusion coefficients for the pristine graphite and 2Zn–graphite composite electrodes, which exhibit distinct patterns for each anode material.

$$I_p = 2.69 \times 10^5 \, AC \, (n^3 \nu D)^{1/2} \tag{1}$$

Fig. S3 (ESI†) shows the first cycle of charge/discharge of the UC–graphite and 2Zn–graphite anodes, with various scan rates of 1 mV s^{-1}, 0.5 mV s^{-1}, 0.25 mV s^{-1}, and 0.1 mV s^{-1}, demonstrating how the peak width decreased as the scan rate was reduced. The anodic peaks became wider as the scan rate increased, and the lithium insertion/de-insertion became delayed. The irreversible capacity loss indicated by the performance in Fig. 3a–e and Fig. S3 (ESI†) can be reduced by modifying the graphite surface with ZnO ALD, because of the structure of graphite, lithium ions could move to the edges and diffuse inside the parallel layers during cycling, and the ZnO nanoparticles are normally located on the edges with defects, which are also Li ion insertion sites; this aids in lithium-ion diffusion, which controlled the SEI layer and accelerated the lithiation and de-lithiation processes that allowed for more Li-ions to be extracted from the modified anode.[8] The differences in current peak amplitudes shown in Fig. 3a, b and Fig. S3 (ESI†) are due to slight variations in experimental conditions during sample preparation and measurement. While Fig. 3a and b show data obtained under controlled and consistent conditions, Fig. S3 (ESI†) includes a broader measurement range for further context. Despite these differences, the observed trend of a more effective current response in the

Table 1 Calculated D_{Li}^{+} values of the pristine graphite and 2Zn–graphite composite electrodes

Electrodes	D_{Li}^{+} (cm^2 s^{-1}) – anodic peaks	D_{Li}^{+} (cm^2 s^{-1}) – cathodic peaks
UC–graphite	1.1×10^{-11}	4.9×10^{-12}
2Zn–graphite	1.8×10^{-11}	7.5×10^{-12}

2Zn–graphite sample over UC–graphite is consistent and reliable. Furthermore, minor changes in the measurement setup or experimental bias may lead to these small variations. However, these characteristics do not impact the overall conclusion of the enhanced performance of 2Zn–graphite. Adding a small quantity of nanoparticles, especially those smaller than 15 nm, to the electrode material could greatly minimize the diffusion distance of lithium ions.[36,40] As ions can intercalate and de-intercalate more quickly from the electrode material, this shorter path allows for faster kinetics. The CV helps understand the redox reactions, faradaic behavior, and charge storage mechanisms within the electrode material. The findings help to characterize and comprehend the composite's potential as an anode material for lithium-ion batteries.

To describe the enhanced functionality and durability of the composite anode material, we evaluated the EIS data. A semicircle and a line in the Nyquist plot correspond, respectively, to the high-medium frequency and low-frequency bands. When the semicircle is in the middle-frequency region, it is linked to the charge transfer resistance (R_{ct}) of the Li-ion intercalation into the electrode. The interfacial layer resistance (R_f), which is attributed to Li-ion diffusion through the SEI layer, solution resistance, and resistances from connections and the current collector, is associated with the high-frequency region. The Warburg impedance, or W_0, which is associated with Li-ion diffusion in the solid substance, is represented by the linear section in the Nyquist plot.[5,11]

As shown in Fig. 4, R_{ct} recorded in composite electrodes is considerably lower than that of UC–graphite, which is attributed to the greater number of intercalation sites.[6,40,41] The smaller semicircle width, seen in Fig. 4b–d, is a sign that R_{ct} of the ZnO modified graphite has dropped. As Fig. 4a shows, the semicircle is wider for UC–graphite due to the high resistance of the dense SEI layer and reduced ionic conductivity of graphite.[3,22,42–45] For all ZnO–graphite composite electrodes, the resistance is reduced because ZnO can enhance the ionic conductivity of the SEI layer by providing pathways for lithium-ion transport. This ensures efficient charge transfer, reduces impedance, and minimizes side reactions, contributing to the overall stability and performance of the SEI layer. The minimized
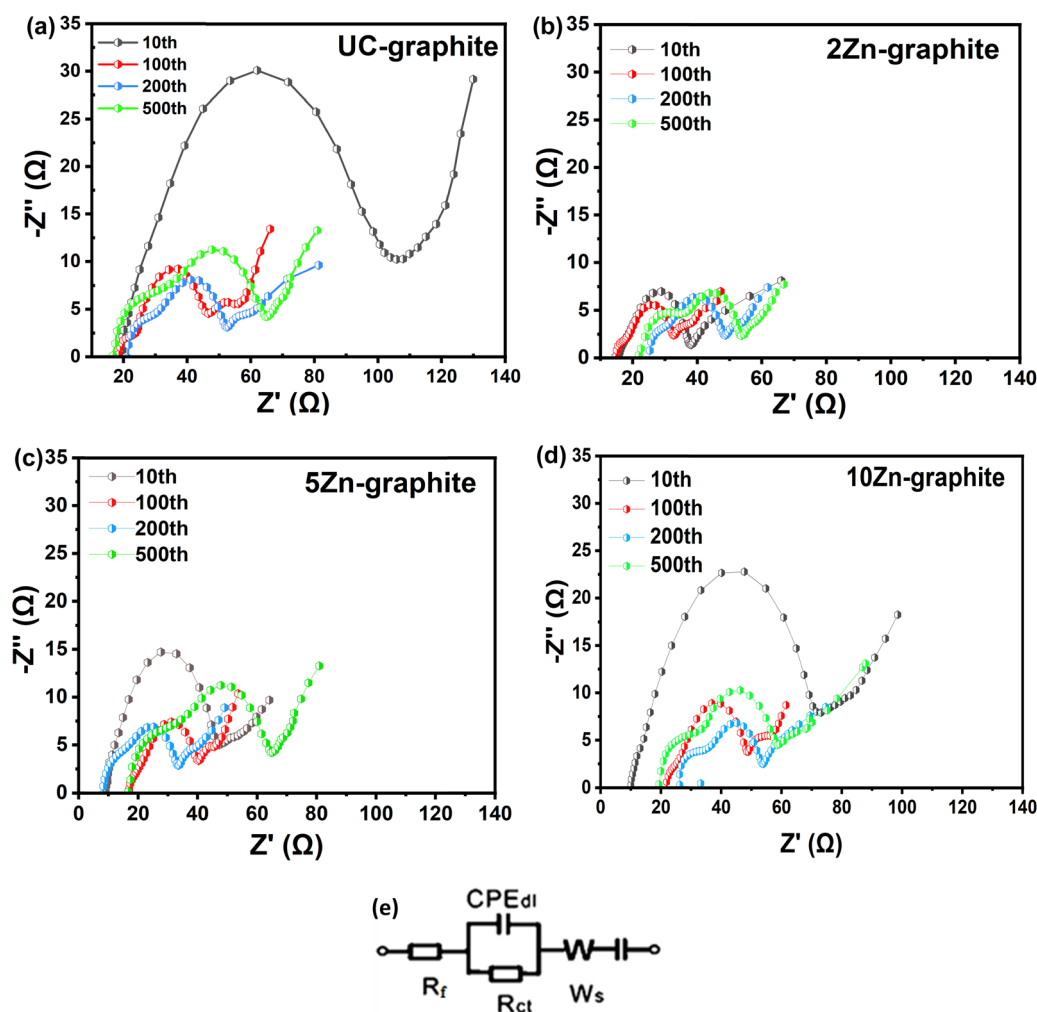

Fig. 4 Nyquist plots of anode samples tested at a 1C rate with a potential range of 0.1–3.0 V at the 10th, 100th, 200th, and 500th charge/discharge cycles for (a) UC–graphite, (b) 2Zn–graphite, (c) 5Zn–graphite, and (d) 10Zn–graphite, and (e) the electrical equivalent circuit model.

side reactions suppressed dendrite growth, enabling a stable and homogeneous SEI layer to form. This finding is supported by the XPS data, which indicate that the 2Zn–graphite formed fewer byproducts. The reason is that 2Zn–graphite has the lowest resistance, which maximizes ion transport during electrochemical reactions and thus the Li-ion diffusion performance in the composite anode. To better understand the electrochemical mechanisms and the impact of the ZnO ALD on the performance of the graphite electrode in lithium-ion batteries, Fig. S4 (ESI†) compares the composite and pristine graphite electrodes after normalizing the Nyquist plots.

When the number of ZnO ALD cycles was larger than 2, larger ZnO nanoparticles were formed, as is shown in Fig. S2 (ESI†), which might increase irreversible capacity. When nanoparticles aggregate, the resulting clusters that operate similarly to larger particles do not effectively accommodate the volume expansion that occurs during ions' insertion and extraction. This aggregation limits the effective surface area accessible for reactions and may increase resistance in the electrode material.[4,36,39] Therefore, maintaining suitable nanoparticle sizes and quantities is critical for sustaining their nanoscale advantages and preventing particle agglomeration, as is displayed in Fig. S2 (ESI†).

Interestingly, the low cycle number of ZnO ALD shows a different trend, implying that the presence of a low amount of ZnO may contribute to more consistent and stable interfacial properties. The cycle number-dependent response underlines the role of ZnO amounts in determining long-term electrode–electrolyte interface stability. The variation in R_f can be attributed to dynamic changes at the electrode–electrolyte interface during prolonged cycling.[3,22,42–44] The initial decrease in R_f may be attributed to the SEI layer's altering features, such as reorganization or improved Li-ion transport, as the system stabilizes under protracted cycle circumstances.[14] However, the following increase in R_f shows that the SEI layer may have been degraded or altered, resulting in increased interfacial resistance. As seen in Fig. 4e, an equivalent circuit was used to match the Nyquist plot for the ZnO–graphite battery.

Galvanostatic charge/discharge measurements were used to further assess the electrochemical characteristics of pristine graphite and ZnO–graphite composite electrodes. To evaluate the long-term stability and discharge capacity of the modified graphite, a longer charge/discharge cycling test was performed on graphite and ZnO–graphite composite electrodes at a current rate of 0.2C for 500 cycles (as shown in Fig. 5a). Fig. 5b depicts the discharge capacity during Li-ion insertion/extraction at various current rates at room temperature. Fig. 5c and d show the 1st, 2nd, 5th, and 10th discharge/charge curves of UC–graphite and 2Zn–graphite, respectively, at a 0.2C rate. As seen in Fig. 5c, pristine graphite provided only 275.6 mA h g^{-1}, which is 74% of the theoretically expected capacity.[46] In our study, the stable 2Zn–graphite composite exhibited a capacity that surpassed the theoretical capacity value of graphite when used as a standalone material, since part of the discharge capacity was contributed by ZnO, which has a theoretical discharge capacity (987 mA h g^{-1}) nearly three times that of graphite. The observed outcome aligns
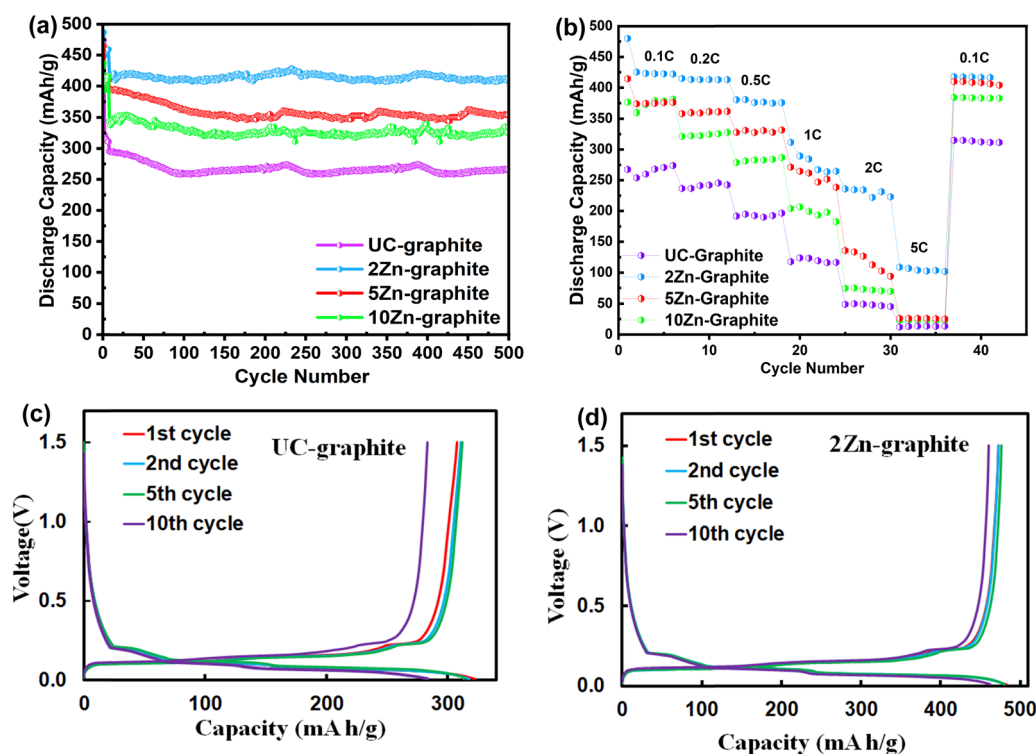

Fig. 5 (a) Cycling performance of graphite anode materials at a 0.2C rate after 500 cycles of charge/discharge, (b) rate performance of graphite anode materials. The 1st, 2nd, 5th, and 10th discharge/charge curves of (c) UC–graphite and (d) 2Zn–graphite at a current rate of 0.2C.

with findings from prior studies involving ZnO–ALD.[9,11,30] ZnO–graphite composites can often exhibit higher discharge capacity due to the contribution of ZnO. The coulombic efficiency (CE) values for graphite electrodes are presented in Fig. S5 (ESI†). The initial CE reflects the extent of lithium-ion loss during the initial cycles, which is primarily due to SEI formation and irreversible side reactions at the electrode surface. For the UC–graphite electrode, the initial CE was $\sim 85\%$, indicating significant lithium consumption during the formation of a thick and unstable SEI. In contrast, the ZnO-coated graphite electrodes exhibited a higher initial CE value of $> 92\%$, which minimizes irreversible lithium consumption by promoting the formation of a compact and stable SEI.

In its first discharge cycle, the 2Zn–graphite electrode exhibited a discharge capacity of 483 mA h g^{-1}, as shown in Fig. 5d, even though the discharge capacity gradually dropped as the current rate increased, as shown in Fig. 5b. This suggests that the ZnO ALD inhibited further SEI formation, improved the battery's initial electrochemical performance, and helped minimize capacity loss during multiple charge/discharge cycles, as shown in Fig. 5c and d. The increased capacity was attributed to the ZnO nanoparticles with the increased number of reaction intercalation sites. According to recent studies, ZnO nanoparticles can lead to higher specific capacities and improved cycling stability due to shorter diffusion pathways, reduced overpotential, and reduced polarization effects. ZnO films with a larger number of ALD cycles can mask a larger graphite surface and reduce the active material utilization, which aligns with findings from prior studies.[47,48] All the composite electrodes proved to be stable except for the 10Zn–graphite electrode; it became unstable when the discharge capacity started to decline rapidly; the instability is attributed to the excessive amount of ZnO, which allows nanoparticles to aggregate and thus may not effectively accommodate the mechanical stresses and avoid volume changes that occur during cycling. This could result in a decrease in stable capacity. Despite the high current rate of 5C, as shown in Fig. 5b, the 2Zn–graphite had the greatest discharge capacity, around 420 mA h g^{-1}, with almost 100% reversibility when it reverted to the 0.1C current rate. The rate performance of the 2Zn–graphite electrode was compared to that of related graphite-based anodes studied in recent years, as summarized in Table S1 (ESI†). The 2Zn–graphite electrode exhibited a specific capacity of 109 mA h g^{-1} at 5C, which is superior to that of bare graphite reported in other studies. This improvement can be attributed to the ZnO ALD treatment, which stabilized the SEI and enhanced cycling performance. While ZnO ALD treatment effectively enhanced SEI stability and suppressed side reactions, further optimization is required to improve charge transfer kinetics and ionic conductivity at high rates. Future strategies could involve combining ZnO ALD with conductive additives, such as graphene, or refining the electrode microstructure to enhance ion and electron transport under high-rate conditions.

SEM was used to investigate the surface morphology of the UC–graphite and 2Zn–graphite electrodes, which will reflect the effects of ZnO ALD on the electrochemical durability of the electrodes. Optimizing the graphite surface morphology can produce anode materials with higher discharge capacities, higher energy densities, higher rate capabilities, and extended lifespans. SEM images of fresh and cycled electrodes from open coin cells were obtained to reveal the microstructure of the particles and their bonding characteristics. The SEM images show small particles on the fresh UC–graphite and 2Zn–graphite electrodes, which are PVDF and carbon black particles in the electrode paste, shown in Fig. 6a and b.

After 100 cycles of charge/discharge, the UC–graphite particles' surfaces became smooth, which was attributed to a partially thick SEI and the byproducts of electrolyte decomposition, as shown in Fig. 6c. In contrast, the 2Zn–graphite electrode had a similar morphology to the fresh electrode because the deposited ZnO nanoparticles resulted in a relatively thin SEI layer on the electrode surface. The presence of ZnO could reduce the decomposition of the electrolyte on the electrode surface by providing a stable and protective interface. This reduces the formation of undesirable by-products that can deteriorate the SEI layer after charge/discharge cycling, as seen in Fig. 6d. In general, due to changes in the surface morphology of these electrodes, pristine graphite tends to generate a rough and uneven SEI layer on the interface, which is unstable and might result in high lithium ion loss during cycling. To study the stability of the SEI layer during long-term cycling, TEM images of cycled UC–graphite and 2Zn–graphite electrodes were taken after 500 charge/discharge cycles (Fig. S6, ESI†). The UC–graphite electrode's SEI layer thickness was measured to be between 35 nm and 80 nm, while the 2Zn–graphite electrode displayed a substantially lower SEI thickness of 7 nm to 30 nm. The 2Zn–graphite electrode's thinner SEI layer shows how well the ZnO ALD treatment suppressed excessive electrolyte decomposition during cycling and stabilized the electrode interface. These SEM and TEM images confirmed that the anode material's efficacy could be improved with only 2 cycles of ZnO ALD. As a result, during the charge/discharge cycling, the resistance decreased, and ion transportation enhanced, increasing the Li-ion diffusion of 2Zn–graphite. Smaller ZnO particles can mitigate volume expansion and contraction during charge/discharge cycling, which helps maintain electrode integrity and prolong battery life. This has been corroborated by various studies,[2,8,23,40,48,49] indicating that smaller nanoparticles reduce mechanical stress and prevent the formation of cracks, leading to more stable cycling behavior.[9,30] The findings point to the successful deposition of ZnO on graphite with minimal agglomeration, ensuring that the nanoparticles maintain their nanoscale features throughout the sample.

XPS was used to determine the surface composition and examine the chemical bonding. Fig. S7 (ESI†) shows the survey scan of UC–graphite electrode and 2Zn–graphite electrode after 100 cycles of charge/discharge. The fitted C1s spectra of the electrode materials are shown in Fig. 7a–c. The C1s spectra of all the electrodes can be deconvoluted into several components, with peaks of C–C species at 284.80 eV for all the electrode materials, and the C=C peaks were observed only for the fresh 2Zn–graphite electrode and the 2Zn–graphite powder, as shown in Fig. S8a (ESI†). The O–C=O species were observed in UC–graphite and fresh 2Zn–graphite electrodes, at 288.63 eV and
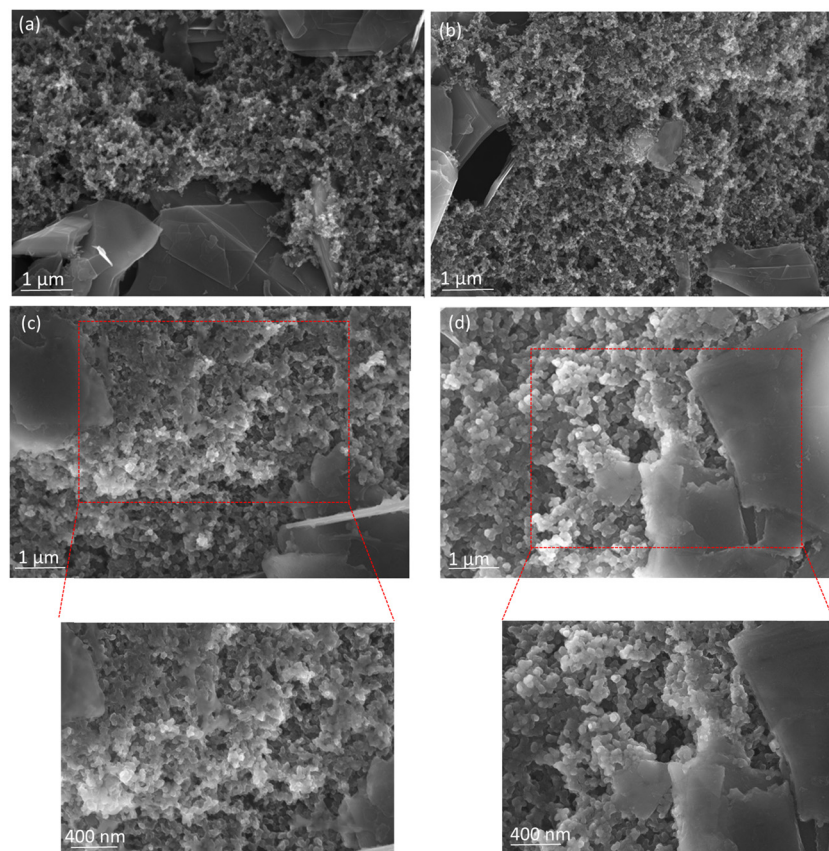
Fig. 6   SEM images of (a) and (c) UC–graphite and (b) and (d) 2Zn–graphite in (a) and (b) their fresh state and (c) and (d) after 100 charge/discharge cycles at a 0.2C rate.

287.28 eV, respectively, which belong to the adventitious carbon.[4] A pair of peaks were detected in the UC–graphite electrode, at 289.84 eV and 286.59 eV, which belong to CF_2 and CH_2, respectively; these peaks were from PVDF, which was used as a binder for the active material. As shown in Fig. 7b and c, CF_2 and CH_2 peaks also appeared for fresh 2Zn–graphite at 290.96 eV and 288.18 eV and for the cycled 2Zn–graphite electrode at 289.25 eV and 288.4 eV, which indicates that side reactions have been efficiently suppressed, and the binder material was redistributed during cycling.[22,50] The two most significant peaks that were detected at around 285.50 eV in both fresh and cycled 2Zn–graphite electrodes may relate to the formation of a –C–O–Zn bond between hydroxyl groups (–O–H) on the graphite, with O–H coming from water used as a precursor in the ALD process. Another peak at 290.09 eV for the UC–graphite electrode is linked to electrolyte decomposition products, such as R–O–Li, which were deposited on the graphite electrode surface.

The O1s spectra confirmed that, under the oxygen deficient atmosphere of the ALD process, more oxygen vacancies might be created in fresh and cycled 2Zn–graphites than in the pristine graphite.[9,11] The spectra revealed distinct shifts and changes in the oxygen binding environment, which may be indicative of the formation of oxygen vacancies. The core level O1s spectra are presented in Fig. 7e and f, with the binding energies of the core peaks of powder and cycled 2Zn–graphite electrode being 531.55 eV and 532.35 eV, respectively, attributed to the formation of ZnO nanoparticles on the graphite particles, and the same peak was observed for the fresh 2Zn–graphite electrode before cycling, as shown in Fig. S8b (ESI†). The same core peak was observed for the UC–graphite electrode at 531.86 eV, as shown in Fig. 7d, with a slight shift attributed to the hydroxyl (–C=O) group. The binding energies of the surface hydroxyl group in the fresh and cycled 2Zn–graphite electrodes were found at 534.19 eV and 533.50 eV, respectively; these values were both higher than that of the UC–graphite electrode (531.96 eV). We observed additional peaks at around 533.20 eV for the cycled UC–graphite electrode, which are assigned to the O^{2-} deficiency and/or R–O–Li species, and another peak assigned to C–O–C species at 534.78 eV.[8,9] The species responsible for these peaks could lead to more electrolyte decomposition, enhance the formation of the SEI layer, and increase its thickness as well. However, we detected two additional peaks for the 2Zn–graphite electrode in the same binding energy range, at 532.51 eV and 534.67 eV, which are attributed to C–O–Zn and –COOH, respectively. C–O–Zn was the result of chemical bonding between Zn and C via O in the Zn–graphite-based electrode material and created an effective interfacial interaction. The presence of –COOH might result from residual water or hydroxyl groups on the surface.[11] As a result,
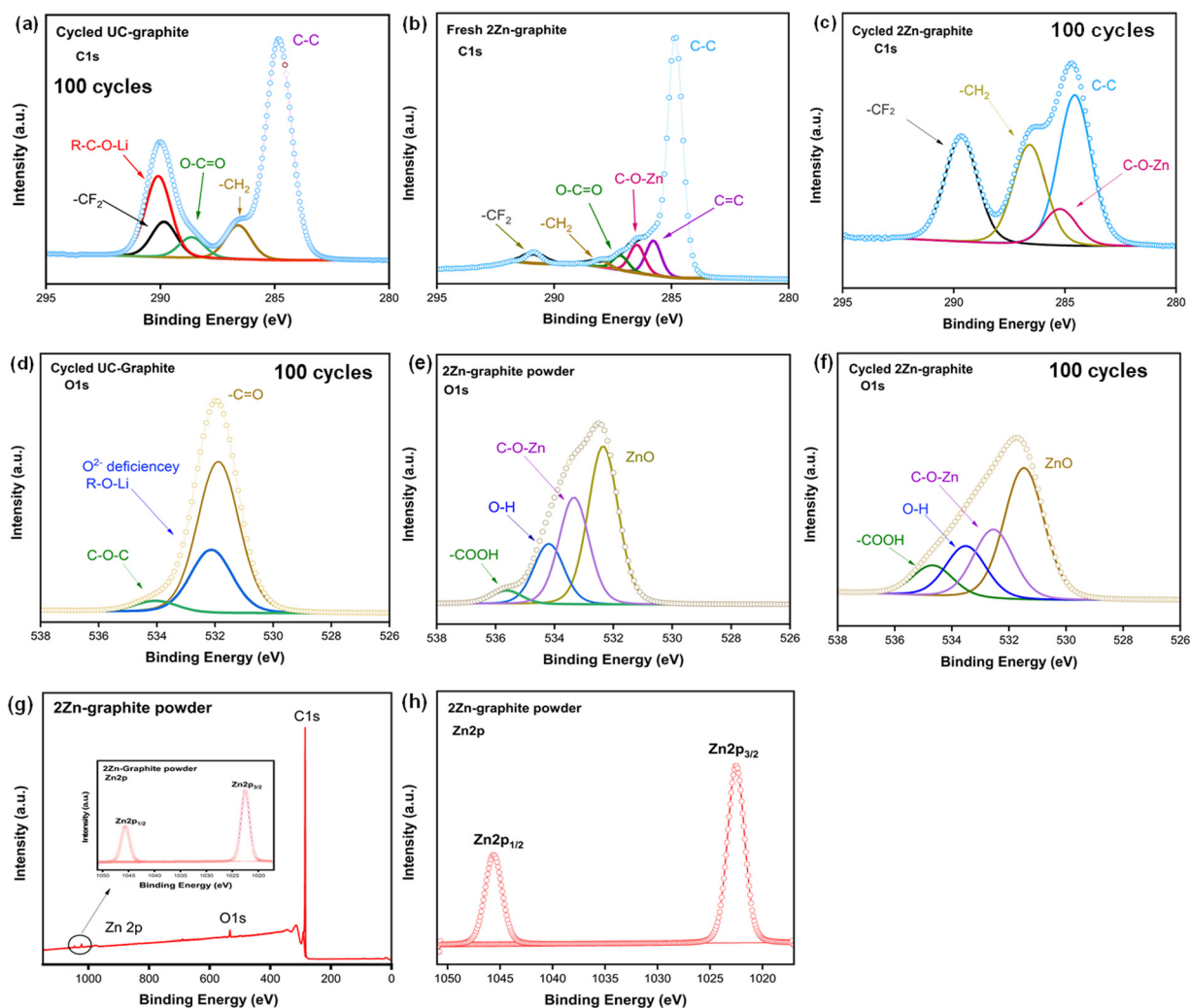
Fig. 7 C1s XPS spectra of (a) cycled UC–graphite electrode after 100 cycles of charge/discharge, (b) fresh 2Zn–graphite electrode, and (c) cycled 2Zn–graphite electrode after 100 cycles of charge/discharge. O1s spectra of (d) cycled UC–graphite electrode after 100 cycles of charge/discharge and (e) and (f) fresh and cycled 2Zn–graphite electrodes. (g) Survey scan XPS spectra of the 2Zn–graphite powder and (h) Zn 2p spectra of the 2Zn–graphite powder.

2Zn–graphite can suppress side reactions, enhance the intercalation/de-intercalation process, and boost the battery's reversible capacity during cycling.

A survey scan of the 2Zn–graphite powder is shown in Fig. 7h, and the Zn 2p spectra of 2Zn–graphite powder and cycled 2Zn–graphite electrode are shown in Fig. 7g and Fig. S7b (ESI†), respectively. The corresponding core level spectra of the Zn 2p3/2 and Zn 2p1/2 states were fitted around 1022.53 eV and 1045.62 eV, respectively. These findings indicate that ZnO ALD effectively enhanced the surface properties of graphite particles while also minimizing side reactions by tuning the amount of ZnO on graphite particles. The F1s spectra of UC–graphite electrode and fresh and cycled 2Zn–graphite electrodes are displayed in Fig. S9 (ESI†). The inorganic components within the SEI layer can be identified from the fitted findings. The main component following the charge/discharge process was LiF, which was generated by electrolyte decomposition and had peaks at 684.95 eV and 684.73 eV for 2Zn–graphite and

UC–graphite electrodes, respectively. In contrast, such peaks were not observed for the fresh 2Zn–graphite electrode. A PVDF peak was observed at 687.71 eV for the fresh 2Zn–graphite electrode before the electrolyte was added. UC–graphite and 2Zn–graphite electrodes also have PVDF peaks at 687.03 eV and 686.71 eV, respectively, from PVDF introduced as a binder; due to the electrolyte, an extra peak at around 687 eV, attributed to $LiPF_6$, was seen for both samples. The EDS mapping in Fig. S10 (ESI†) shows the spatial distribution of Zn, F, P, and C elements on the surface of the 2Zn–graphite electrode after 500 cycles of charge/discharge. The consistent distribution of Zn suggests that the ZnO ALD coating persisted during cycling, potentially stabilizing the electrode interface or integrating into the SEI layer. The XPS results are consistent with the findings from EIS and TEM analysis. ZnO ALD nanoparticles could reduce side reactions on the anode's surface, suppress electrolyte decomposition, and reduce the initial irreversible capacity loss. XPS and SEM analyses show that the SEI layer in the UC–graphite

electrode was thick and not homogeneous. These analyses show that 2Zn–graphite can reduce the SEI thickness and promote its homogeneity.

Conclusions

Side reactions caused by electrolyte decomposition would result in the irreversible loss of lithium and the formation of SEI layers, which would decrease a battery's capacity over time. In this study, a low amount of ZnO deposited by ALD increased the SEI layer's uniformity and electrochemical durability. According to the electrochemical studies of samples with various numbers of ZnO ALD cycles, the discharge capacity declined with the increasing amount of ZnO, reaching a maximum stable capacity with 2 cycles of ZnO ALD. The 2Zn–graphite composite sample demonstrated excellent charge/discharge cycling performance and a high discharge capacity. The SEI layer's stability problem was resolved, and its electrochemical stability was improved by applying ZnO nanoparticles. This study highlights the potential of improving commercial graphite anode materials with surface modification. The findings of this study can help the development of various devices with stable, long lasting battery performance.

Authors' contributions

X. L. conceived and supervised the project. A. H. and H. Y. designed the experiments. A. H. carried out all experiments. A. H. and X. L. wrote the main manuscript. All authors reviewed the manuscript.

Data availability

All data are provided in the manuscript and ESI† files.

Conflicts of interest

The authors have declared that they have no competing financial interests.

References

1 J. P. Pender, G. Jha, D. H. Youn, J. M. Ziegler, I. Andoni and E. J. Choi, *et al.*, Electrode degradation in lithium-ion batteries, *ACS Nano*, 2020, **14**(2), 1243–1295, DOI: **10.1021/acsnano.9b04365**.

2 S. T. Plunkett, C. Chen, R. Rojaee, P. Doherty, Y. S. Oh and Y. Galazutdinova, *et al.*, Enhancing thermal safety in lithium-ion battery packs through parallel cell current dumping mitigation, *Appl. Energy*, 2021, **286**, 116495, DOI: **10.1016/j.apenergy.2021.116495**.

3 R. Xu, X.-B. Cheng, C. Yan, X.-Q. Zhang, Y. Xiao and C.-Z. Zhao, *et al.*, Artificial interphases for highly stable lithium metal anode, *Matter*, 2019, **1**(2), 317–344, DOI: **10.1016/j.matt.2019.05.016**.

4 J. Gnanaraj, R. W. Thompson, S. Iaconatti, J. DiCarlo and K. Abraham, Formation and growth of surface films on graphitic anode materials for Li-ion batteries, *Electrochem. Solid-State Lett.*, 2005, **8**(2), A128, DOI: **10.1149/1.1850390**.

5 C. Wang, A. J. Appleby and F. E. Little, Charge–discharge stability of graphite anodes for lithium-ion batteries, *J. Electroanal. Chem.*, 2001, **497**(1–2), 33–46, DOI: **10.1016/S0022-0728%2801%2900708-2**.

6 B. Suthar, P. W. Northrop, D. Rife and V. R. Subramanian, Effect of porosity, thickness and tortuosity on capacity fade of anode, *J. Electrochem. Soc.*, 2015, **162**(9), A1708, DOI: **10.1149/2.0061509jes**.

7 L. Chen, K.-S. Chen, X. Chen, G. Ramirez, Z. Huang and N. R. Geise, *et al.*, Novel ALD chemistry enabled low-temperature synthesis of lithium fluoride coatings for durable lithium anodes, *ACS Appl. Mater. Interfaces*, 2018, **10**(32), 26972–26981, DOI: **10.1021/acsami.8b04573**.

8 Y. Li, Y. Zhao, G. Huang, B. Xu, B. Wang and R. Pan, *et al.*, ZnO nanomembrane/expanded graphite composite synthesized by atomic layer deposition as binder-free anode for lithium ion batteries, *ACS Appl. Mater. Interfaces*, 2017, **9**(44), 38522–38529, DOI: **10.1021/acsami.7b11735**.

9 Y. Lin, Z.-H. Huang, X. Yu, W. Shen, Y. Zheng and F. Kang, Mildly expanded graphite for anode materials of lithium ion battery synthesized with perchloric acid, *Electrochim. Acta*, 2014, **116**, 170–174, DOI: **10.1016/j.electacta.2013.11.057**.

10 N. Li, S. Jin, Q. Liao and C. Wang, ZnO anchored on vertically aligned graphene: binder-free anode materials for lithium-ion batteries, *ACS Appl. Mater. Interfaces*, 2014, **6**(23), 20590–20596.

11 S. Lu, H. Wang, J. Zhou, X. Wu and W. Qin, Atomic layer deposition of ZnO on carbon black as nanostructured anode materials for high-performance lithium-ion batteries, *Nanoscale*, 2017, **9**(3), 1184–1192, DOI: **10.1039/C6NR07868K**.

12 L. Gao, J. Li, J. Ju, L. Wang, J. Yan and B. Cheng, *et al.*, Designing of root-soil-like polyethylene oxide-based composite electrolyte for dendrite-free and long-cycling all-solid-state lithium metal batteries, *Chem. Eng. J.*, 2020, **389**, 124478, DOI: **10.1016/j.cej.2020.124478**.

13 Y. Jin, Z. Zheng, D. Wei, X. Jiang, H. Lu and L. Sun, *et al.*, Detection of micro-scale Li dendrite via H$_2$ gas capture for early safety warning, *Joule*, 2020, **4**(8), 1714–1729, DOI: **10.1016/j.joule.2020.05.016**.

14 B. Liu, J.-G. Zhang and W. Xu, Advancing lithium metal batteries, *Joule*, 2018, **2**(5), 833–845, DOI: **10.1016/j.joule.2018.03.008**.

15 K. Liu, Y. Liu, D. Lin, A. Pei and Y. Cui, Materials for lithium-ion battery safety, *Sci. Adv.*, 2018, **4**(6), eaas9820, DOI: **10.1126/sciadv.aas9820**.

16 K. Liu, R. Zhang, J. Sun, M. Wu and T. Zhao, Polyoxyethylene (PEO)|PEO–perovskite| PEO composite electrolyte for all-solid-state lithium metal batteries, *ACS Appl. Mater. Interfaces*, 2019, **11**(50), 46930–46937, DOI: **10.1021/acsami.9b16936**.

17 W. Shu, Z. Jian, J. Zhou, Y. Zheng and W. Chen, Boosting the electrochemical performance of Li$_{1.2}$Ni$_{0.13}$Co$_{0.13}$Mn$_{0.54}$O$_2$ by

rough coating with the superionic conductor $Li_7La_3Zr_2O_{12}$, *ACS Appl. Mater. Interfaces*, 2021, **13**(46), 54916–54923, DOI: **10.1021/acsami.1c14229**.

18 H. Yang, C. Guo, A. Naveed, J. Lei, J. Yang and Y. Nuli, *et al.*, Recent progress and perspective on lithium metal anode protection, *Energy Storage Mater.*, 2018, **14**, 199–221, DOI: **10.1016/j.ensm.2018.03.001**.

19 Q. Yang, Q. Li, Z. Liu, D. Wang, Y. Guo and X. Li, *et al.*, Dendrites in Zn-based batteries, *Adv. Mater.*, 2020, **32**(48), 2001854, DOI: **10.1002/adma.202001854**.

20 B. H. Hou, Y. Y. Wang, Q. L. Ning, W. H. Li, X. T. Xi and X. Yang, *et al.*, Self-supporting, flexible, additive-free, and scalable hard carbon paper self-interwoven by 1D microbelts: superb room/low-temperature sodium storage and working mechanism, *Adv. Mater.*, 2019, **31**(40), 1903125, DOI: **10.1002/adma.201903125**.

21 J. Li, H. Fu, M. Gu, J. Chen, J. Zhou and L. Fan, *et al.*, Ether-based gel polymer electrolyte for high-voltage potassium ion batteries, *Nano Lett.*, 2024, **24**(37), 11419–11428, DOI: **10.1021/acs.nanolett.4c02168**.

22 J. Qian, B. D. Adams, J. Zheng, W. Xu, W. A. Henderson and J. Wang, *et al.*, Anode-free rechargeable lithium metal batteries, *Adv. Funct. Mater.*, 2016, **26**(39), 7094–7102, DOI: **10.1002/adfm.201602353**.

23 Y. Chen, X. Chen and Y. Zhang, A csomprehensive review on metal-oxide nanocomposites for high-performance lithium-ion battery anodes, *Energy Fuels*, 2021, **35**(8), 6420–6442, DOI: **10.1021/acs.energyfuels.1c00315**.

24 Y.-N. Li, C.-Y. Wang, R.-M. Gao, F.-F. Cao and H. Ye, Recent smart lithium anode configurations for high-energy lithium metal batteries, *Energy Storage Mater.*, 2021, **38**, 262–275, DOI: **10.1016/j.ensm.2021.03.016**.

25 Y. Hu, H. Fu, Y. Geng, X. Yang, L. Fan and J. Zhou, *et al.*, Chloro-functionalized ether-based electrolyte for high-voltage and stable potassium-ion batteries, *Angew. Chem.*, 2024, **136**(23), e202403269, DOI: **10.1002/ange.20243269**.

26 Z. Xu, Y. Zhao, M. Li, Z. Li, J. Li and Y. Song, *et al.*, Stable and improved voltage plate of $Li/SOCl_2$ battery using carbon electrodes with active carbon, *Phys. Scr.*, 2024, **99**(6), 065044, DOI: **10.1088/1402-4896/ad4a9b**.

27 Y. Jin, H. Yu and X. Liang, Simple approach: Heat treatment to improve the electrochemical performance of commonly used anode electrodes for lithium-ion batteries, *ACS Appl. Mater. Interfaces*, 2020, **12**(37), 41368–41380, DOI: **10.1021/acsami.0c10823**.

28 C. Lim, B. Yan, H. Kang, Z. Song, W. C. Lee and V. De Andrade, *et al.*, Analysis of geometric and electrochemical characteristics of lithium cobalt oxide electrode with different packing densities, *J. Power Sources*, 2016, **328**, 46–55, DOI: **10.1016/j.jpowsour.2016.07.119**.

29 E. Quartarone, V. Dall'Asta, A. Resmini, C. Tealdi, I. G. Tredici and U. A. Tamburini, *et al.*, Graphite-coated ZnO nanosheets as high-capacity, highly stable, and binder-free anodes for lithium-ion batteries, *J. Power Sources*, 2016, **320**, 314–321, DOI: **10.1016/j.jpowsour.2016.04.107**.

30 M. Yu, A. Wang, Y. Wang, C. Li and G. Shi, An alumina stabilized ZnO–graphene anode for lithium ion batteries via atomic layer deposition, *Nanoscale*, 2014, **6**(19), 11419–11424, DOI: **10.1039/C4NR02576H**.

31 H. Yu, Y. Gao and X. Liang, Slightly fluorination of Al_2O_3 ALD coating on $Li_{1.2}Mn_{0.54}Co_{0.13}Ni_{0.13}O_2$ electrodes: Interface reaction to create stable solid permeable interphase layer, *J. Electrochem. Soc.*, 2019, **166**(10), A2021, DOI: **10.1149/2.0951910jes**.

32 M. K. Aslam, Y. Niu, T. Hussain, H. Tabassum, W. Tang and M. Xu, *et al.*, How to avoid dendrite formation in metal batteries: innovative strategies for dendrite suppression, *Nano Energy*, 2021, **86**, 106142, DOI: **10.1016/j.nanoen.2021.106142**.

33 D. Hu, L. Chen, J. Tian, Y. Su, N. Li and G. Chen, *et al.*, Research progress of lithium plating on graphite anode in lithium-ion batteries, *Chin. J. Chem.*, 2021, **39**(1), 165–173, DOI: **10.1002/cjoc.202000512**.

34 K. N. Wood, M. Noked and N. P. Dasgupta, Lithium metal anodes: toward an improved understanding of coupled morphological, electrochemical, and mechanical behavior, *ACS Energy Lett.*, 2017, **2**(3), 664–672, DOI: **10.1021/ACSEnergyLett.6B00650**.

35 A. Helaley, G. D. Zhan and X. Liang, Tailored PEO/PEG-PPG polymer electrolyte for solid-state lithium-ion battery, *J. Electrochem. Soc.*, 2024, **171**(11), 110509, DOI: **10.1149/1945-7111/ad8d80**.

36 Z. Wang, G. Dang, Q. Zhang and J. Xie, Xanthan gum as a potential binder for graphite anode in lithium-ion batteries, *Int. J. Electrochem. Sci.*, 2017, **12**(8), 7457–7468, DOI: **10.20964/2017.08.55**.

37 Y. Gao, X. He, L. Ma, T. Wu, J. Park and X. Liang, Understanding cation doping achieved by atomic layer deposition for high-performance Li-ion batteries, *Electrochim. Acta*, 2020, **340**, 135951, DOI: **10.1016/j.electacta.2020.135951**.

38 A. L. Hoskins, W. W. McNeary, S. L. Millican, T. A. Gossett, A. Lai and Y. Gao, *et al.*, Nonuniform growth of sub-2 nanometer atomic layer deposited alumina films on lithium nickel manganese cobalt oxide cathode battery materials, *ACS Appl. Nano Mater.*, 2019, **2**(11), 6989–6997, DOI: **10.1021/acsanm.9b01490**.

39 Y. Cao, X. Meng and A. Li, Atomic layer deposition of high-capacity anodes for next-generation lithium-ion batteries and beyond, *Energy Environ. Mater.*, 2021, **4**(3), 363–391, DOI: **10.1002/eem2.12132**.

40 V. S. Rangasamy, S. Thayumanasundaram and J.-P. Locquet, Solid polymer electrolytes with poly (vinyl alcohol) and piperidinium based ionic liquid for Li-ion batteries, *Solid State Ionics*, 2019, **333**, 76–82, DOI: **10.1016/J.SSI.2019.01.024**.

41 Y. Wang, X. Jiang, L. Yang, N. Jia and Y. Ding, *In situ* synthesis of C/Cu/ZnO porous hybrids as anode materials for lithium ion batteries, *ACS Appl. Mater. Interfaces*, 2014, **6**(3), 1525–1532, DOI: **10.1021/am404181q**.

42 C. Chen, S. Plunkett, M. Salameh, S. Stoyanov, S. Al-Hallaj and M. Krishnamurthy, Enhancing the fast charging capability of high-energy-density lithium-ion batteries: A pack design perspective, *IEEE Electrif. Mag.*, 2020, **8**(3), 62–69, DOI: **10.1109/MELE.2020.3005700**.

43 J. Lin, X. Liu, S. Li, C. Zhang and S. Yang, A review on recent progress, challenges and perspective of battery thermal management system, *Int. J. Heat Mass Transfer*, 2021, **167**, 120834, DOI: **10.1016/j.ijheatmasstransfer.2020.120834**.

44 J. Tan, A. Cannon and E. Ryan, Simulating dendrite growth in lithium batteries under cycling conditions, *J. Power Sources*, 2020, **463**, 228187, DOI: **10.1016/j.jpowsour.2020.228187**.

45 H. Usui, T. Kono and H. Sakaguchi, Novel composite thick-film electrodes consisted of zinc oxide and silicon for lithium-ion battery anode, *Int. J. Electrochem. Sci.*, 2012, **7**(5), 4322–4334, DOI: **10.1016/S1452-3981(23)19541-1**.

46 Y. Jin, H. Yu, Y. Gao, X. He, T. A. White and X. Liang, $Li_4Ti_5O_{12}$ coated with ultrathin aluminum-doped zinc oxide films as an anode material for lithium-ion batteries, *J. Power Sources*, 2019, **436**, 226859, DOI: **10.1016/j.jpowsour.2019.226859**.

47 C. Wang, Q. Sun, Y. Liu, Y. Zhao, X. Li and X. Lin, *et al.*, Boosting the performance of lithium batteries with solid-liquid hybrid electrolytes: Interfacial properties and effects of liquid electrolytes, *Nano Energy*, 2018, **48**, 35–43, DOI: **10.1016/j.nanoen.2018.03.020**.

48 A. W. Weimer, Particle atomic layer deposition, *J. Nanopart. Res.*, 2019, **21**(1), 9, DOI: **10.1007/s11051-018-4442-9**.

49 G. Kalimuldina, A. Nurpeissova, A. Adylkhanova, D. Adair, I. Taniguchi and Z. Bakenov, Morphology and dimension variations of copper sulfide for high-performance electrode in rechargeable batteries: A review, *ACS Appl. Energy Mater.*, 2020, **3**(12), 11480–11499, DOI: **10.1021/acsaem.0c01686**.

50 H. Yu, X. He and X. Liang, AlF_3-Al_2O_3 ALD thin-film-coated $Li_{1.2}Mn_{0.54}Co_{0.13}Ni_{0.13}O_2$ particles for lithium-ion batteries: Long-term protection, *ACS Appl. Mater. Interfaces*, 2022, **14**(3), 3991–4003, DOI: **10.1021/acsami.1c20005**.